Heavy Ion Reaction Cross Sections

C.A. BERTULANI*

Institut für Kernphysik, Kernforschungsanlage Jülich, D-5170 Jülich, West Germany

Recebido em 17 de fevereiro de 1986

Abstract We evaluate the reaction cross sections of heavy ion collisions for $E_{lab}/A > 30$ MeV and we put emphasis on the effects of the Pauli principle and of the electromagnetic excitations. Both effects are shown to be of great importance and can be handled by means of simple geometrical and semiclassical ideas.

1. INTRODUCTION

Heavy ion collisions at intermediate and high energies are a subject of increasing experimental and theoretical interest[1]. Very little is known experimentally about the physics of such highly charged particle collisions. In order to study the reactions in this realm some basic quantities as the total reaction cross sections are of useful information for the design of future accelerators and experiments[2].

Normally the data are compared with the standard geometrical overlap model which assumes that the total reaction cross section must be proportional to the squared sum of the radii of the ions. Deviations from this crude approximation are guessed to come from transparency effects[3] and from the electromagnetic contribution to the fragmentation of the nuclei[4].

Our purpose in this paper is to develop a microscopic calculation, which starts from the experimental data on nucleon-nucleon free cross sections, in order to describe the nuclear contribution to the total reaction cross sections of heavy ion collisions with laboratory energy above 30 MeV per nucleon. We make a detailed study of the effect of the Pauli principle for intermediate energy collisions up to

*On leave of absence from the Universidade Federal do Rio de Janeiro, Brasil, and supported by the Deutscher Akademischer Austauschdienst/CAPES.

300 MEV/A and the inclusion of the electromagnetic fragmentation mechanism is performed by means of the recent theoretical results of Refs. 5 and 6. To that aim we start in section 2 with an analysis of the effect of the Pauli principle in the binary collisions between the nucleons of a two-nuclear-matter system in relative motion. We show that it reduces to a geometrical problem in the momentum space of the system and an analytical derivation for it is presented in the appendix. The results of such a derivation are used in section 3, together with the Boltzmann equation, to proceed to a study of the approach to equilibrium of the two-nuclear-matter system. These calculations are intended to give a clearer insight on this subject and are useful in the analysis of nucleus-nucleus collisions.

In section 4 we develop a semiclassical derivation of the heavy ion cross sections whose inputs are the results of section 2. In section 5 we add the contribution of the electromagnetic interactions and we make a comparison with the geometric overlap model for the cross sections of a special group of reactions. The regions of influence of the nucleon-nucleon collisions and of the electromagnetic effects are inferred.

2. PAULI BLOCKING IN NUCLEAR MATTER COLLISIONS

The effect of Pauli blocking, i.e. Pauli principle, in nucleon-nucleus collisions was first investigated by Goldberger[7] and by Clementel and Villi[8] on the basis of the geometry for a single nucleon-nucleon collision in momentum space. Their approach is still used in the microscopic descriptions of nucleon-nucleus cross sections with good agreement with the experimental data (see e.g. Ref. 9). We will show how one can extend their ideas to the study of the collision between two nuclear matters.

The fundamental input of the calculations is the free nucleon-nucleon cross section σ_{NN}^{free}. Fig. 1 displays the interpolated curves for the experimental data[10,11] of σ_{NN}^{free} as a function of the laboratory energy

$$E_{lab} = \sqrt{\hbar^2 k_{lab}^2 c^2 + m^2 c^4} - mc^2 \qquad (2.1)$$

The energy dependence of the cross sections can be qualitatively described by

$$\sigma_{NN}^{free} \propto \frac{1}{E_{lab}} \quad \text{for} \quad E_{lab} < 100 \text{ MeV} \tag{2.2a}$$

and

$$\sigma_{NN}^{free} \propto \text{constant} \quad \text{for} \quad E_{lab} \geq 100 \text{ MeV} \tag{2.2b}$$

Goldberger's work is based upon the approximation (2.2b) and Clementel and Villi's work upon the approximation (2.2a). We shall use these prescriptions to proceed to a qualitative study of the effect of Pauli blocking in nuclear matter collisions, before we use the interpolation of the experimental data presented in fig. 1 for a more quantitative analysis.

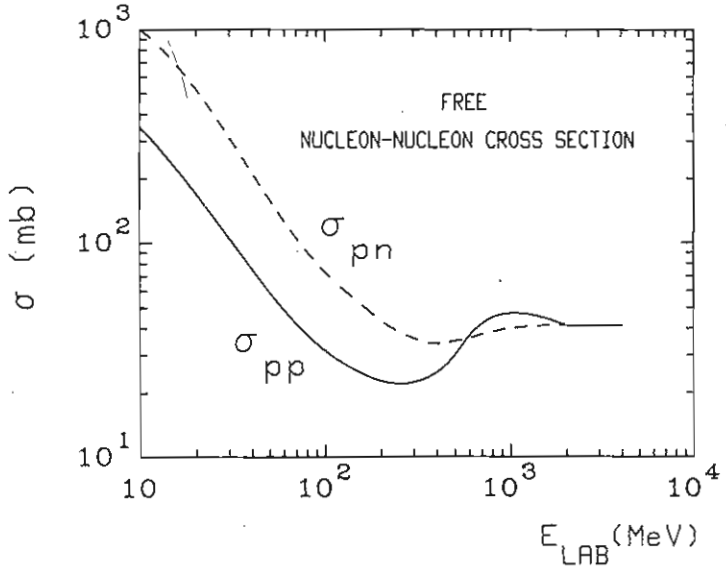

Fig.1 - Free nucleon-nucleon cross section as a function of the laboratory energy. The Coulomb contribution has been removed in σ_{pp}.

By nuclear matter collisions we mean two Fermi fluids, one of which is initially as rest and the other is moving against the first with a momentum $\vec{k}_{lab} = \vec{k}_0$ per nucleon. Each of these fluids possesses a Fermi motion in its rest frame and the initial state of the system is described by two filled spheres of radii $k_{F_>}$ and $k_{F_<}$, corresponding respectively to the larger and smaller spheres, with the position of their centers separated by k_0, as shown in fig. 2. In the initial stage of the system a binary collision between a pair of nucleons will only be possible if they pertain to different Fermi fluids. If initially they have momenta $\vec{k}_1$ and $\vec{k}_2$, after the collision they will possess momenta $\vec{k}_1'$ and $\vec{k}_2'$, which by the Pauli principle must lie outside both Fermi spheres. These momenta are also related by the energy-momentum conservation laws

$$\begin{aligned} \vec{k}_1 \; \vec{k}_2 &= \vec{k}_1'+\vec{k}_2' \\ \vec{k}_1'-\vec{k}_2' &= \hat{\varepsilon}|\vec{k}_1-\vec{k}_2| \end{aligned} \tag{2.3}$$

where $\hat{\varepsilon}$ is a unit vector in the direction of a solid angle $d\Omega$. We observe that the conservation of the energy of relative motion in the binary collision is only valid for energies below the pion-threshold $E_{lab} \simeq 300$ MeV above which most of the collision cross section will be inelastic due to pion production. Nevertheless, we shall see that for relative motion energy of the Fermi fluids greater than this value the Pauli principle has a rapidly decreasing importance and the above assumption can be used without major consequences.

In fig. 2 we observe that, due to the Pauli principle and the conservation laws (2.3), the available solid angle $4\pi\omega_S$ for scattering of the pair is restricted to the non-hatched region inside the auxiliary sphere of radius $q = |\vec{k}_1-\vec{k}_2|/2$. To this solid angle not only a pair but all pairs of nucleons can scatter which lie on the surface of this auxiliary sphere and inside the double-hatched region of fig. 2. This double-hatched region forms a solid angle $4\pi\omega_I$. The calculation of ω_S and ω_I is of great relevance in our following analysis and we show that it can be translated into a beautiful problem of spherical geometry.

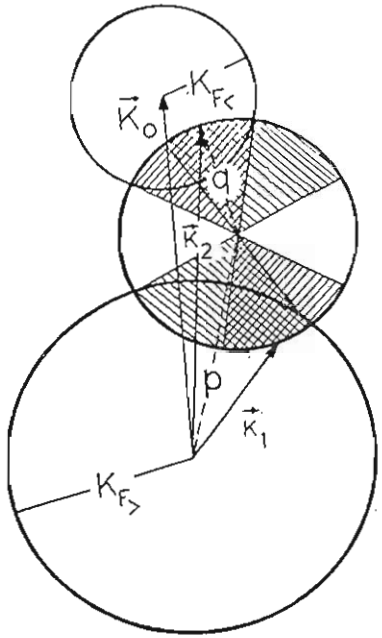

Fig. 2 - Diagram exhibiting the kinematics of the two nucleon collision. The initial momenta of the pair, $\vec{k}_1$ and $\vec{k}_2$, together with $\vec{k}_0$, $\vec{p}$ and $\vec{q}$ are represented by arrows as indicated. The third sphere is the locus of the end points of the vector $\vec{q}'$. The non-shaded region corresponds to the allowed scattering angle. The cross-hatched region indicates the admissible angles for initial pairs with the same total momentum $2p$ and the same modulus $2q$ for the relative momentum.

We present the solution to this problem in the appendix where analytical expressions are deduced for $\omega_S(\vec{k}_1,\vec{k}_2,k_0,k_{F_>},k_{F_<})$ and $\omega_I(\vec{k}_1,\vec{k}_2,k_0,k_{F_>},k_{F_<})$.

In order to measure the effect of the Pauli blocking upon the nucleon-nucleon cross section in the Fermi fluid media we define the averaged quantity

$$\sigma_{NN}^{\text{bound}} = \left(\frac{4}{3}\pi k_{F_>}^3\right)^{-1}\left(\frac{4}{3}\pi k_{F_<}^3\right)^{-1}\int_{F_>}\int_{F_<} d^3k_1 d^3k_2\ \omega_S\ \frac{2q}{k_0}\ \sigma_{NN}^{\text{free}} \qquad (2.4)$$

where the integrations are carried out inside different Fermi spheres. The factor ω_S is the fraction of the solid angle available for a specific collision between a nucleon with momentum $\vec{k}_1$ and another with momentum $\vec{k}_2$. The free nucleon-nucleon cross section $\sigma_{NN}^{\text{free}}(E)$ is a function of $\vec{k}_1$ and $\vec{k}_2$ by means of $E = \sqrt{\hbar^2(\vec{k}_1-\vec{k}_2)^2c^2+m^2c^4} - mc^2$. The factor $\frac{2q}{k_0}$ corrects for the flux difference between the laboratory system and a system in which one of the nucleons is at rest. In reality the effect of the Pauli principle must be greater than that expressed by eq. (2.4). This is because we assume that the free nucleon-nucleon cross section is isotropic while it is actually lower at the 90° angle of scattering in the center of mass frame of reference of the pair, specially for p-p collisions, and it is this angular region which contributes mostly to the binary collisions in the two-nuclear-matter system.

Due to the cylindrical symmetry in the momentum space distribution, eq. (2.4) can be reduced to a five-fold integration and the result can be put into the form

$$\sigma_{NN}^{\text{bound}}(E) = P(\xi,\eta)\sigma_{NN}^{\text{free}}(E) \qquad (2.5)$$

where

$$\xi = \frac{k_0}{k_{F_>}} \quad \text{and} \quad \eta = \frac{k_{F_<}}{k_{F_>}} \qquad (2.6)$$

In fig. 3 we present the results of the numerical calculation for P_A and P_B corresponding to the assumptions (2.2a) and (2.2b), respectively. The curves for $\eta = 0$ reproduce exactly the results of Refs. 7 and 8, as it should be. For $\eta = 1$, meaning two colliding nuclear matters of the same density, the Pauli blocking is more effective and there will exist an appreciable reduction of the free nucleon-nucleon cross section up to $k_0/k_F \simeq 5$, i.e., for energy of relative motion per nucleon approximately equal to 17 times the Fermi energy if we take $k_F = 1.35$.

For $\xi < 1+\eta$ the two Fermi spheres overlap and we come to the problem of double-counting of nucleons in the overlap region, which is not allowed by the Pauli principle. One can imagine that the momentum distribution of the nucleons will be somehow rearranged before this impossible situation occurs. We make no such speculations in our calcu-

lations but we suppose that, whatever may happen, the curves of fig. 3 will closely reproduce the average influence of the Pauli blocking in the binary collisions also for $\xi < 1+\eta$. Of course, within this approach, a pair of nucleons whose momenta lie inside this overlap region are not scattered at all, and this leads to an increasing transparency of the nuclear matters with decreasing energy of relative motion. That is why P_A and P_B quickly go to zero for $\xi < 1+\eta$, even in the case $\eta = 1$.

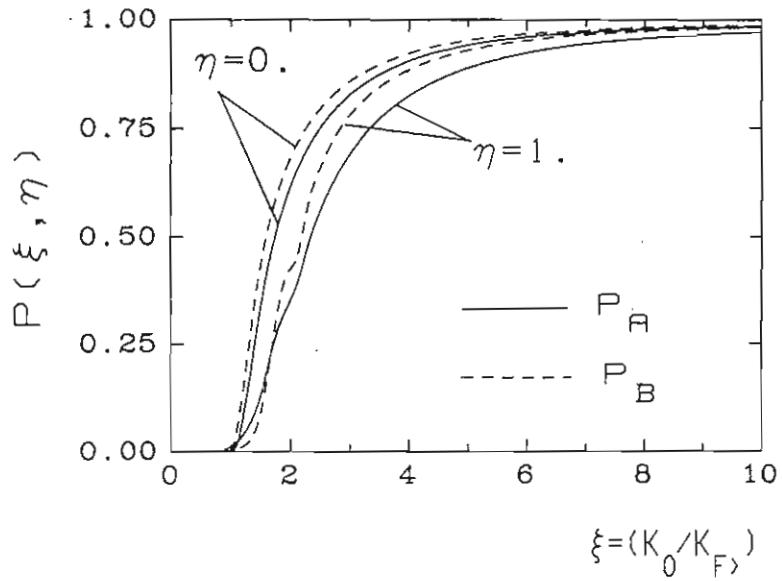

Fig. 3 - The ratio of the average nucleon-nucleon cross section in the two nuclear matter system and its value in free-space. η is the ratio between the smaller and the larger of the Fermi momenta, $k_{F<}$ and $k_{F>}$ respectively. ξ is the ratio between the momentum of relative motion of the system and $k_{F>}$.

3. TIME DEVELOPMENT OF THE MOMENTUM DISTRIBUTION

The binary collisions will modify the momentum distribution of the nucleons, which we shall study by means of the Boltzmann equation. This is a balance equation of the form

$$\frac{\partial f(\vec{k}_1)}{\partial t} = G(\vec{k}_1) - L(\vec{k}_1) \tag{3.1}$$

where the gain and loss terms are respectively

$$G = (1-f_1) \int \frac{d^3k_2}{(2\pi)^3} \; v_{12} \; (1-f_2) \int d\Omega \;\; f_1' f_2' \, \frac{d\sigma}{d\Omega} \tag{3.2}$$

and

$$L = f_1 \int \frac{d^3k_2}{(2\pi)^3} \, v_{12} \, f_2 \int \; d\Omega (1-f_1')(1-f_2') \, \frac{d\sigma}{d\Omega} \tag{3.3}$$

The function $f(\vec{k})$ is the occupation number for the momentum state $\vec{k}$ and we have used in the above equations the short notation

$$f_1' = f(\vec{k}_1'), \text{ etc.}$$

The factor v_{12} is the relative velocity of a given colliding pair of nucleons with momenta $\vec{k}_1$ and $\vec{k}_2$. Eq. (3.1), together with the definitions (3.2) and (3.3) for the gain and loss terms, differs from the classical Boltzmann equation only by the introduction of the Pauli blocking factor[12] $(1-f_1)(1-f_2)$ in the collision integrals.

Just in order to obtain a qualitative view of the time development of the momentum distribution, at least in the initial stage of evolution, we assume an isotropic free nucleon-nucleon cross section and use the parametrizations of eqs. (2.2). The collision of nucleons inside the same sphere is forbidden because of the exclusion principle; therefore, the collision mechanism depletes both spheres simultaneously throwing the colliding pair into the outside region of the Fermi spheres. Within these assumptions the gain and loss terms take the form

$$G = (1-f_1) \int \frac{d^3k_2}{(2\pi)^3} v_{12} \ (1-f_2) \ \omega_I \ \sigma_{NN}^{free} \tag{3.4}$$

and

$$L = f_1 \int \frac{d^3k_2}{(2\pi)^3} v_{12} \ f_2 \ \omega_S \ \sigma_{NN}^{free} \tag{3.5}$$

where

$$\omega_I(\vec{k}_1,\vec{k}_2,\xi,\eta) = \frac{1}{4\pi} \int d\Omega \ f_1' f_2' \tag{3.6}$$

and

$$\omega_S(\vec{k}_1,\vec{k}_2,\xi,\eta) = \frac{1}{4\pi} \int d\Omega (1-f_1')(1-f_2') \tag{3.7}$$

Since $f(\vec{k})$ is initially equal to one if $\vec{k}$ lies inside one of the Fermi spheres, and zero otherwise, eqs. (3.6) and (3.7) are exactly equal to the definitions of ω_I and ω_S given in the last section and whose analytical expressions are deduced in the appendix.

All terms in the integrands of eqs. (3.4) and (3.5) can be written as functions of $\vec{k}_1$, $\vec{k}_2$, ξ and η and the three-fold integrals can be solved numerically. Fig. 4 displays the results of these integrations for $L(\vec{k})$ (fig. 4a) and $G(\vec{k})$ (fig. 4b) and for the parametrization of eq. (2.2b). We have taken $\xi = 2$ and $\eta = 0.5$. Actually the numbers are normalized such that they represent the functions

$$\ell(\vec{k}) = \frac{L(\vec{k})}{\int_F \frac{d^3k}{(2\pi)^3} L(\vec{k})} \quad \text{and} \quad g(\vec{k}) = \frac{G(\vec{k})}{\int_F \frac{d^3k}{(2\pi)^3} L(\vec{k})} \tag{3.8}$$

where the integral in the denominators is carried out inside one of the two Fermi spheres. This integral is equal to the total rate of loss of nucleons inside one sphere and, by conservation of particles, it must be the same in both spheres. Of course, by using the definition (3.8), ℓ and g will be independent of the proportionality constants of eqs. (2.2). The functions $\ell(\vec{k})$ and $g(\vec{k})$ possess cylindrical symmetry in

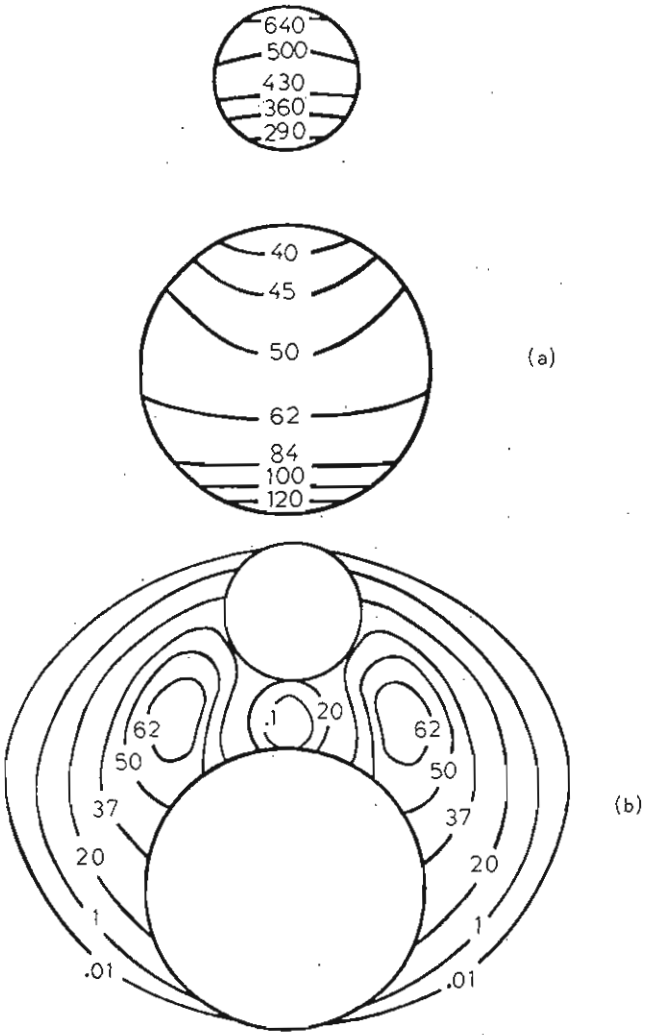

Fig. 4 - The functions $\ell(\vec{k})$ and $g(\vec{k})$, normalized according to eqs. (3.8) and for $\xi = 2.0$ and $\eta = 0.5$. Apart from the two circles that indicate the contour of the two Fermi spheres, the curves exhibited are lines of constant value of ℓ and g with the corresponding value indicated over the line. This pattern corresponds to the use of the parametrization (2.2b).

$\vec{k}$-space and we plotted in fig. 4 the curves of constant values of ℓ and g. In fig, 4a we observe that, because of the more available scattering angle, the binary collisions are more favoured for pairs of nucleons with larger relative momentum $|\vec{k}_1-\vec{k}_2|$ and this is reflected in the fact that the rate of loss $\ell(\vec{k})$ is greater in the opposite extremes of the Fermi spheres. In fig. 4b we see that the nucleons are preferentially scattered in a direction perpendicular to the momentum $\vec{k}_0$ of relative motion of the Fermi fluids. Their final momenta after the first collisions tend to be concentrated in a toroidal region lying on a plane passing between the two spheres.

In fig. 5 we present the same functions (3.8) but corresponding to the parametrization of eq. (2.2a). We observe that there are two competing mechanisms which produce the pattern exhibited in fig. 5: The exclusion principle favours the depletion of the large relative momentum nucleons and the energy dependence of the cross section favours the small relative momentum collisions. This results in the appearance, in the large sphere, of a region of least probability of collision somewhere near its center. In fig. 5b we exhibit the plots of constant values of g and we note that the effect of preferential scattering perpendicular to $\vec{k}_0$ is stronger than in the case of fig. 4b. Since the parametrization (2.2a) is more proper for low energy collisions, the inclusion of the Pauli principle is shown to be of extreme importance in the analysis of nuclear collisions in the low and intermediate energy regime.

For a more quantitative study of the relaxation of the two nuclear matter system by means of the Boltzmann equation, one can use an interpolation of the experimental data, as the one shown in fig. 1, and make an average over spin and isospin degrees of freedom. The time can be divided into small steps Δt and the momentum distribution at time $t+\Delta t$ is obtained from the distribution at time t by solving eq. (3.1):

$$f(\vec{k},\ t+\Delta t) \simeq f(\vec{k},t) + \Delta t\left(\frac{\partial f}{\partial t}\right)_t \qquad (3.9)$$

Of course, this will be a problem of formidable computational task,

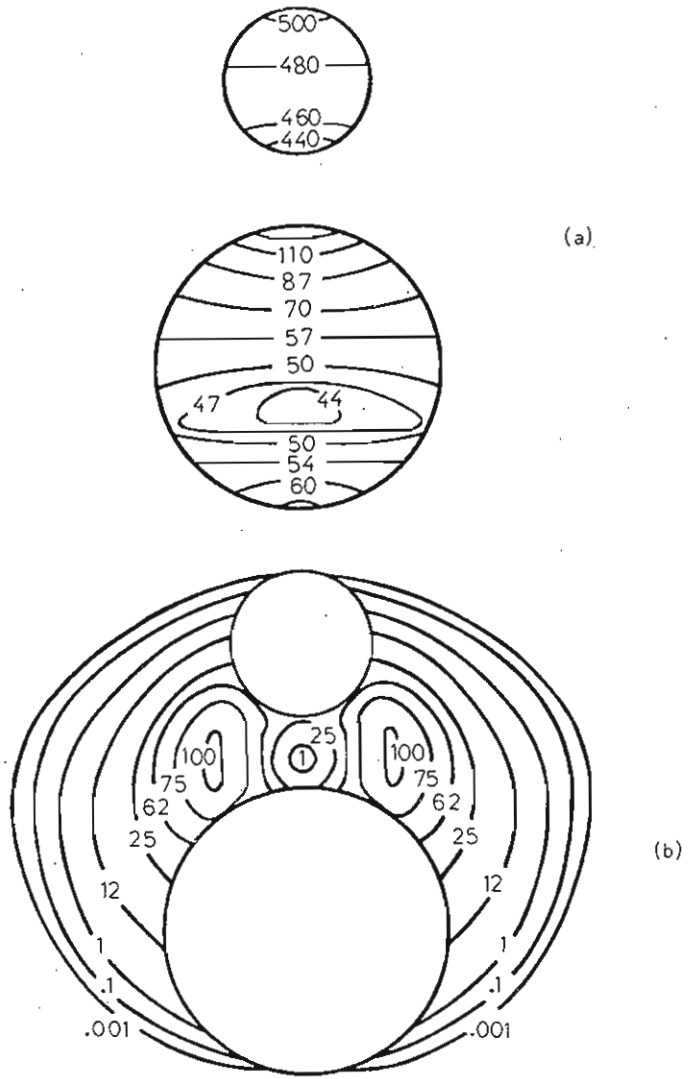

Fig. 5 - The same as fig. 4 but with the parametrization (2.2a).

since the expressions (3.6) and (3.7) are no longer analytical as in the initial stage of evolution of the system, and one is obliged to solve two five-fold integrations, i.e., the eqs. (3.2) and (3.3) at each time step. To obtain the time evolution of a physical quantity one has to perform an additional three-fold integration in the $\vec{k}$-space, which makes the problem of extreme practical difficulty. Nevertheless, one can already infer a lot of information by the use of the solution $(\frac{\partial f}{\partial t})_{t=0}$ for the initial stage of evolution, as we shall demosntrate by means of some reasonable assumptions.

It is clear that for $t \to \infty$ the momentum distribution will tend to a spherically symmetric distribution in the center of mass reference frame of the system. The physical quantities of interest like the total momentum or energy of the relative motion of the system will reach a constant value asymptotically. We make the simplifying assumptions that the nuclear matters possess the same number of protons and neutrons and the same Fermi momentum $k_F = 1.35\ fm^{-1}$, corresponding to saturated nuclear matters. We define

$$\vec{Q} = \left[\frac{2K_F^3}{3\pi^2}\right]^{-1} \int 4f(\vec{k},t)\ \vec{k}\ \frac{d^3k}{(2\pi)^3} - \frac{\vec{k}_0}{2} \qquad (3.10)$$

which is the average relative momentum per nucleon diminished by the center of mass momentum $\vec{k}_0/2$, with respect to the laboratory system of reference (where one of the nuclear matters is initially at rest). The factor 4 multiplying the distribution function $f(\vec{k},t)$ inside the integral accounts for the isospin-spin degeneracy of the nuclear matters. We suppose that this quantity decreases exponentially in time:

$$Q(t) = Q(0)\, e^{-t/\tau} \qquad (3.11)$$

from which it follows that the relaxation time of the system is obtained by

$$\frac{1}{\tau} = -\frac{(dQ/dt)_{t=0}}{Q(0)} = -\frac{12\pi^2}{k_F^3} \int \frac{\vec{k}.\vec{k}_0}{k_0^2} \left(\frac{\partial f}{\partial t}\right)_{t=0} \frac{d^3k}{(2\pi)^3} \qquad (3.12)$$

These assumptions allow us to use eqs. (3.4) and (3.5) to calculate the

initial rate of change $(\frac{\partial f}{\partial t})_{t=0}$ of the momentum distribution. Due to the cylindrical symmetry of $\frac{\partial f}{\partial t}$, eq. (3.12) can be expressed as a five-fold integration which we solved by numerical methods. For the nucleon-nucleon cross section we used

$$\sigma_{NN}^{free}(E) = \frac{1}{2}\left[\sigma_{pp}^{free}(E) + \sigma_{pn}^{free}(E)\right]$$

and the fit of the experimental data of σ_{pp}^{free} and σ_{pn}^{free} displayed in fig. 1.

In fig. 6 we present the results of this numerical integration where τ^{BN} is the relaxation time due to the binary collisions, without accounting for the Pauli principle, which means to put $\omega_S = 1$ in eq. (3.5). The curve assigned by τ^{BNP} is the same calculation but with the inclusion of the Pauli principle. One observes in this figure that the inclusion of the Pauli principle dramatically changes the time development of the two-nuclear-matter system up to energies $E_{lab}/A \simeq 300$ MeV. For low energies the system will be more "transparent" to the binary collisions and the relaxation time can be some orders of magnitude greater than τ^{BN}.

In principle it is of no fundamental difficulty to apply the Boltzmann equation to the analysis of finite-nuclei collisions (see e.g. Ref. 13). But the spatial inhomogeneity complicates the description substantially and, unless some additional simplifications are done, the problem turns to be unpractical.

In the next section we calcule the contribution of the binary collisions to the total heavy ion reaction cross sections. The collisional time τ_{coll}, i.e., the time interval in which the ions are in contact, is about 10 fm/c. We then expect to treat properly the effect of Pauli principle by using the local density approximation as we shall explain there. The use of this approximation is justified because the Pauli principle affects appreciably the cross sections only in the peripheral collisions for which the momentum distributions of the participant nucleons have a relaxation time $\tau^{BNP} \ll \tau_{coll}$, when $E_{lab}/A \lesssim 300$MeV. For higher energies this condition fails but then this approximation will have no more influence on the results, either.

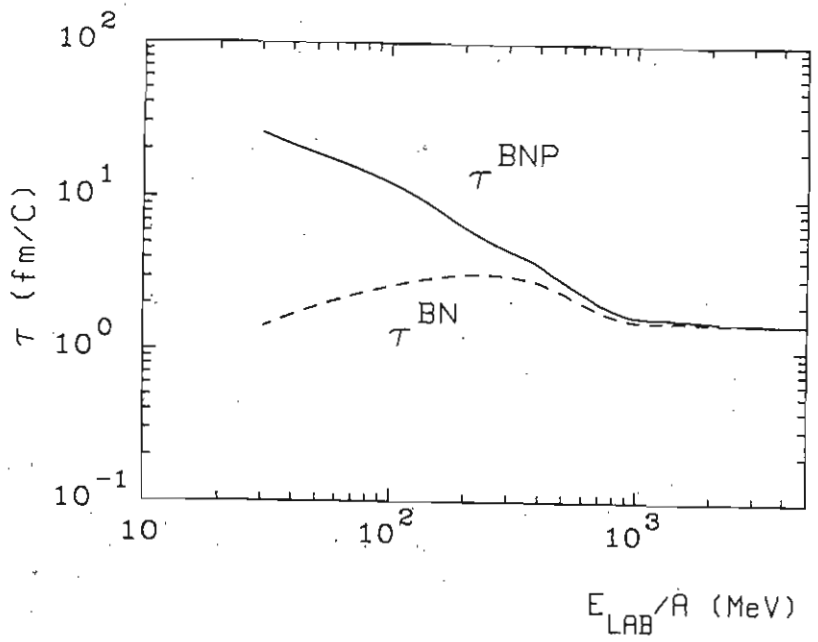

Fig. 6 - Relaxation time of the two nuclear matter system as a function of the laboratory energy per nucleon. The solid (dashed) line includes (does not include) the Pauli principle effect.

4. HEAVY ION COLLISION CROSS SECTIONS

A semi-empirical "black sphere" expression for the reaction cross section of projectile and target nuclei, with mass numbers A_p and A_T, respectively, introduced by Bradt and Peters[14] and extensively used in the literature is

$$\sigma = \pi r_0^2 (A_p^{1/3} + A_T^{1/3} + \delta)^2 \qquad (4.1)$$

The "overlap parameter" δ is meant to represent the diffuseness and partial transparency of the nuclear surfaces. Nevertheless, it was shown

in a recent experiment[2] that the fit of expressions like eq. (4.1) with the data is quite poor. The overprediction at low projectile and/or target masses is thought to be due to nuclear transparency effects and the underprediction at larger masses might be explained by the addition of Coulomb processes.

The effects of nuclear transparency were calculated by DeVries and Peng[3] using the optical limit of Glauber theory. They suggested that the dip of the experimental nucleon-nucleon cross section σ_{NN}^{free} around $E_{lab} \simeq 200$ MeV should be reflected in the heavy ion total reaction cross sections, provided that bulk effects (e.g. collective excitations, hydrodynamic effects, etc.) do not play a dominant role, and they were able to reproduce the experimental data for light projectiles such as protons, α-particles, He and deuterons in various target nuclei. Nevertheless, effects of Pauli principle and Coulomb fragmentation were not included which could substantially modify their results, specially for larger projectile and target masses.

We follow a similar path here, only we base ourselves on semi-classical ideas without explicit relation with the Glauber theory. We also include Pauli principle and Coulomb effects. Our fundamental assumption is the local density approximation by means of which we can associate local Fermi momenta to each point inside the space overlap region of the two ions by

$$K_{F_{1,2}}(\vec{r}) = \left(\frac{3\pi^2}{2}\rho_{1,2}\right)^{1/3} \qquad (4.2)$$

where $\rho_1(\rho_2)$ is the nuclear matter density of the projectile (target) at the position $\vec{r}$. We use the mass density experimentally determined by electron scattering or muonic level measurements over the periodic table[15]

$$\rho(r) = \rho_0/\{1 + \exp[(r-R_D)/a_D]\} \qquad (4.3a)$$

with

$$R_D = 1.12\, A^{1/3} - 0.86\, A^{-1/3}\ fm \qquad (4.3b)$$

$$a_D = 0.54\ fm$$

The mass density is normalized by

$$\int \rho d^3r = A, \quad \text{so that} \quad \rho_0 = 0.17\ fm^{-3} \tag{4.3c}$$

The projectile is assumed to move in a straight line with constant velocity $\vec{v}$ and we do not consider the recoil of the target nucleus. In a semiclassical sense we can say that in a nucleon-nucleus reaction the probability that the nucleon goes through the nucleus without suffering any binary collision is given by

$$T_n = \exp\left(-\int \frac{dz}{\lambda(z)}\right) \tag{4.4}$$

where

$$\lambda = (\rho\ \sigma_{NN}^{\text{bound}})^{-1}$$

is the local mean free path of the incident nucleon inside the nucleus. We extend this formulation to the case of nucleus-nucleus collisions by taking the total transmission probability of the projectile passing through the target as the product of the transmission probability T_n for each projectile nucleon separately. The following expression results

$$T = \exp\left\{-\int \frac{dz}{\Lambda(z,b)}\right\} \tag{4.5a}$$

where

$$\Lambda^{-1}(z,b) = \int \rho_1\rho_2\ \sigma_{NN}^{\text{bound}}\ d^3r \tag{4.5b}$$

and b is the impact parameter of the heavy ion collision. We use the parametrization of eq. (2.5) for the bound nucleon-nucleon cross sections with $P = P_A$ when $E_{lab}/A < 100$ MeV and $P = P_B$ when $E_{lab}/A \geq 100$MeV.

Of course, $\sigma_{NN}^{\text{bound}}$ will depend on the local densities ρ_1 and ρ_2 through eq. (4.2); to account, at least partially, for the nuclear charge symmetry we take the isospin averaged cross section

$$\sigma_{NN} = \frac{1}{A_P A_T}\left[(Z_P Z_T + N_P N_T)\sigma_{pp} + (Z_P N_T + Z_T N_P)\sigma_{pn}\right] \tag{4.6}$$

For an application we choose the particular reactions (a) $^{40}Ca + {}^{40}Ca$; (b) $^{40}Ca + {}^{238}U$; and (c) $^{238}U + {}^{238}U$.

In fig. 7 we display the opacity function for each of these reactions, defined by

$$\text{Opac.} = 1 - T(b) \tag{4.7}$$

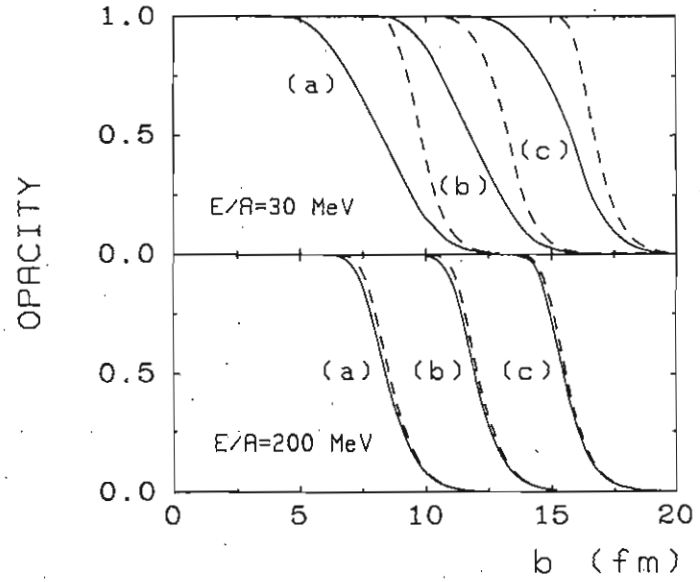

Fig. 7 - The opacity function of the impact parameter and for the three chosen reactions (a) $^{40}Ca + {}^{40}Ca$; (b) $^{40}Ca + {}^{238}U$, and (c) $^{238}U + {}^{238}U$. The solid (dashed) line include (do not include) the Pauli principle effect.

and which measures the reaction probability as a function of the impact parameter b. The dashed lines correspond to the neglect of the Pauli principle and the solid ones include the Pauli principle. One notes that there is an appreciable difference between the two curves for lower laboratory energies. This is primarily a surface effect since for central collisions there is no probability that the nuclei will maintain their identities after the scattering. This does not mean, however, that the influence of the Pauli principle is limited to peripheral collisions because, as we saw in section 3, it will greatly affect the angular distributions of the scattered nucleons, principally in the regions of higher nuclear mass densities which are involved in the central collisions. The spectra of nucleons emitted during the early stages of a nuclear collision (the knock-out nucleons[16]) must reflect the structure of these angular distributions.

The total reaction cross sections are obtained by

$$\sigma^N = 2\pi \int b\left[1-T(b)\right]db \qquad (4.8)$$

where the index N indicates that it is from nuclear interaction origin. In fig. 8 we present the reaction cross sections in barns for the three chosen reactions and as a function of the laboratory energy per nucleon E_{lab}/A in MeV. The dashed curves correspond to the neglect of the Pauli principle. It is clear that these curves must have a form similar to the nucleon-nucleon cross sections because of the way they were deduced. The solid curves include the Pauli principle and we observe that for energies $E_{lab}/A \lesssim 300$ MeV they are shifted downwards relative to the first ones due to a larger transparency of the ions to binary collisions.

The dip in the cross sections around $E_{lab}/A = 200$ MeV is not as pronounced as in fig. 1 and it does not create more than a 5% deviation from an average constant value. Without appreciable error we take the high-energy limit for this average value, which for the reaction (a) is 2.6 barns, for the reaction (b) is 5.0 barns and for the reaction c) is 8.2 barns. If we try to fit these numbers to the relation

(4.1) we find, using $r_0 = 1.2$ *fm*, that $\delta = 0.74$ for (a), $\delta = 0.92$ for (b) and $\delta = 1.1$ for (c). Thus the concept of a geometrical cross section, as implied by eq. (4.1), is useless. This is because one assumes a sharp cutoff radius for the nuclei and tries to account for surface effects by means of the quantity δ. But for larger-mass targets the projectile will have to overcome a greater path length as it moves through the nuclear density tail of the target and the reaction probability will be greater than that corresponding to lighter nuclei. Thus δ must vary with A_P and A_T.

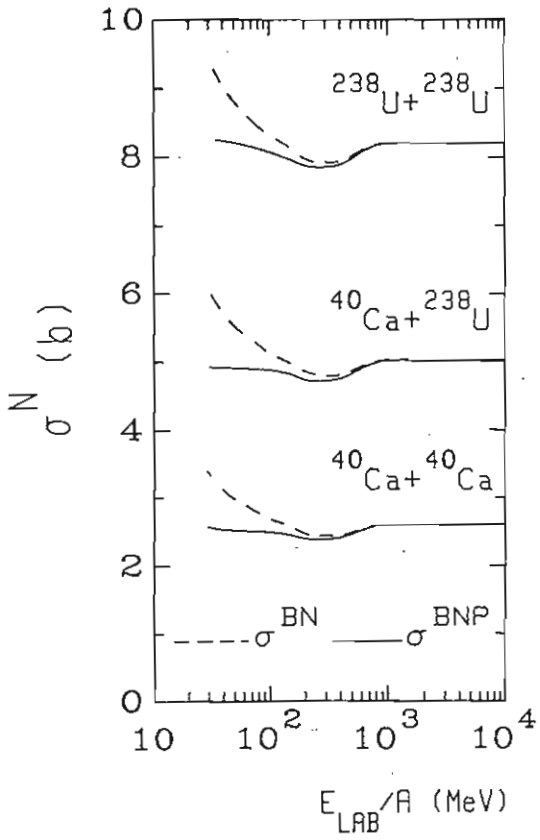

Fig. 8 - Nuclear contributions to the total reaction cross sections as functions of the laboratory energy per nucleon. The solid (dashed) lines include (do not include) the Pauli principle effect.

The contribution of electromagnetic effects is not included in eq. (4.1), either. It is already known[4] that this contribution increases with increasing nuclear charges and with increasing E_{lab}/A. In the next section we show how this contribution can be incorporated easily in the total reaction cross sections.

5. ELECTROMAGNETIC EFFECTS

A standard way of studying the electromagnetic effects in relativistic heavy ion collisions is the use of the Weizsäcker-Williams approximation[17] which properly accounts for the electric dipole excitation of the ions. But the inclusion of other multipolarities of excitation is also very important and recently an extension of the Weizsäcker-Williams method to include all other multipolarities was accomplished[5,6]. In this theory the excitation cross section of one nucleus by an energy amount $\hbar\omega$ due to the electromagnetic interaction with the other nucleus is given by

$$\sigma^C = \sum_{\ell} \int \{ n_{E\ell}(\omega)\sigma^{ph}_{E\ell}(\omega) + n_{M\ell}(\omega)\sigma^{ph}_{M\ell}(\omega) \} \frac{d\omega}{\omega} \tag{5.1}$$

where $n_{E/M\ell}(\omega)$ is the equivalent number of photons with the frequency ω (also called by virtual photon numers) of the electric or magnetic radiation and multipolarity ℓ. They are given in an analytical form in Ref. 5. The functions $\sigma^{ph}_{E/M\ell}(\omega)$ are the photonuclear absorption cross sections for the excitation energy $\hbar\omega$.

In high energy collisions the electromagnetic excitation is a very sudden process and the excited states concentrate in a narrow region around the socalled giant resonances. These resonances normally decay by particle emission or by fission, thus also contributing to the fragmentation of the nuclei. We shall study here only the effects of the most important resonances, namely the electric dipole $E1$ and the electric quadrupole $E2$ giant resonances. We quote from Ref. 5:

$$n_{E1}(\omega) = Z^2\alpha \frac{2}{\pi}\left(\frac{c}{v}\right)^2 \left[\xi K_0 K_1 - \frac{v^2\xi^2}{2c^2}(K_1^2 - K_0^2)\right] \tag{5.2a}$$

$$n_{E2}(\omega) = Z^2\alpha \frac{2}{\pi}\left(\frac{c}{v}\right)^4 \left[2\left(1 - \frac{v^2}{c^2}\right) K_1^2 + \xi\left(2 - \frac{v^2}{c^2}\right)^2 K_0 K_1 + \frac{\xi^2}{2}\left(\frac{v}{c}\right)^4 (K_0^2 - K_1^2)\right] \tag{5.2b}$$

where Z is the projectile charge (for target excitations) or the target charge (for projectile excitations), α is the fine-structure constant, v is the relative velocity of the ions, c is the speed of light, and K_n are the modified Bessel functions of n-th order as functions of

$$\xi = \frac{\omega R}{\gamma c} \tag{5.3}$$

In the above formula γ is the relativistic factor

$$\gamma = (1 - v^2/c^2)^{-1/2} \tag{5.4}$$

and R is the sum of the two nuclear radii. For $\sigma^{ph}_{E\ell}$ we use the theoretical definitions[5]

$$\sigma^{ph}_{E1} = \frac{16\pi^3}{9}\frac{\omega}{c} B(E1) \tag{5.5a}$$

$$\sigma^{ph}_{E2} = \frac{4\pi^3}{75}\left(\frac{\omega}{c}\right)^3 B(E2) \tag{5.5b}$$

where we take the following[18] sum rules for the reduced transition probabilities $B(E\ell)$.

$$B(E1) = 14.8 \frac{NZ}{A}\frac{1}{E_{GR}} \text{ MeV } e^2\ fm^2 \tag{5.6a}$$

$$B(E2) = 50\, Z\, (1.2\, A^{1/3})^2 \frac{1}{E_{GR}} \text{ MeV } e^2\ fm^2 \tag{5.6b}$$

and the charge and atomic numbers are those relative to the excited nucleus. The resonance energy $E_{GR} = \hbar\omega$ is taken to be

$$E_{GR}(\ell = 1) = \frac{80}{A^{1/3}} \text{ MeV} \tag{5.7a}$$

$$E_{GR}(\ell = 2) = \frac{62}{A^{1/3}} \text{ MeV} \tag{5.7b}$$

In fig. 9 we present the cross sections for the excitation of the giant $E1$ and $E2$ resonances of the projectile (P) and of the target (T) due to the electromagnetic interaction between them. The cross sections are given in millibarns and as a function of the laboratory energy per nucleon in MeV. The solid curves represent the sum of al these partial cross sections. We notice that the $E2$ contribution is more important in the intermediate-energy regime and that the $E1$ contribution predominates for high energies, above some hundred MeV per nucleon.

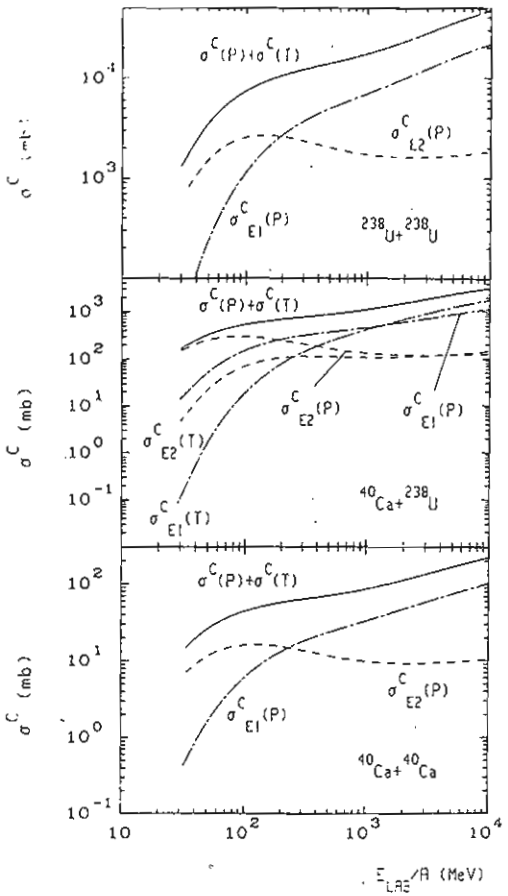

Fig. 9 - Electric dipole ($E1$) and quadrupole ($E2$) excitation cross sections of the giant resonances in the projectile (P) and in the target (T). The solid line represents the sum of all four contributions.

Instead of eqs. (5.5) one could also use the experimentally measured photonuclear fragmentation cross sections in eq. (5.1). Altough most of the experimental results are for the $E1$ cross sections, some information about the $E2$ photonuclear fragmentation cross sections is now becoming available (see e.g. Ref. 19). We expect, however, that eqs. (5.5) and (5.6) are sufficiently good for our purposes.

Adding the nuclear and electromagnetic contributions we find the total reaction cross sections which are illustrated in fig. 10.

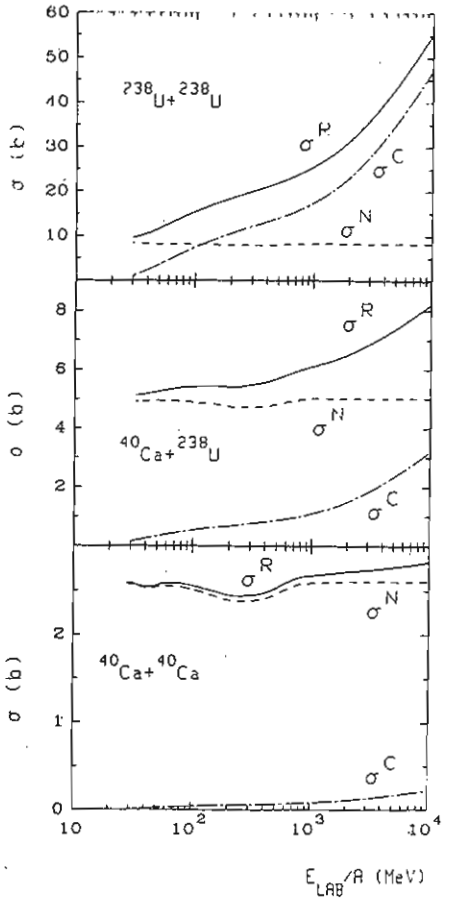

Fig.10 - Comparison between nuclear (σ^N) and electromagnetic (σ^C) contributions to the total reaction cross sections (σ^R).

We observe the increasing importance of the electromagnetic cross sections with increasing energy. We also note that for large mass nuclei the electromagnetic contribution can even become the greatest one for energies above some hundred MeV per nucleon. Of course, there can be no parametrization of the total reaction cross section σ^R as the one implied by eq. (4.1)

6. CONCLUSIONS

Any serious study of heavy ion collisions at intermediate and high energies must include the effects of the Pauli exclusion principle and electromagnetic excitation. The geometrical concept of the reaction cross sections loses its significance when these effects are included. We showed that one can account for the Pauli principle by means of simple geometrical methods as soon as one assumes that the binary collisions between the nucleons are the most important nuclear mechanism in the heavy ion reactions at intermediate and high energies. The electromagnetic contributions must include not only the electric dipole excitations but also other multipolarities and are shown to be of fundamental importance for higher energies and heavier ions.

The author is grateful to Prof. L.C. Gomes for useful discussions and to Dr. G. Baur for a critical reading of the manuscript. He also acknowledges the support and hospitality by Prof. J. Speth at the Kernforschungsanlage Jülich.

APPENDIX: CALCULATION OF ω_S AND ω_I

We consider the collision between one nucleon of momentum $\vec{k}_1$ from one Fermi fluid with another of momentum $\vec{k}_2$ from the other Fermi fluid. We define

$$\vec{p} = \frac{\vec{k}_1 + \vec{k}_2}{2}$$
$$\vec{q} = \frac{\vec{k}_2 - \vec{k}_1}{2} \qquad (A.1)$$

and

$$\vec{b} = \vec{k}_0 - \vec{p}$$

After the collision $\vec{p}$ and $\vec{b}$ stay constant while $\vec{q}$ changes only its direction.

Fig. 2 of section 2 shows schematically the geometry of the collision. The allowed scattering angle of the pair corresponds to the non-hatched region of the spherical surface with center in $\vec{p}$ and radius equal to q. This angle is equal to $4\pi\omega_S$, according to the definition given in section 2. The possible angle of origin of nucleon-pairs with the same momentum $\vec{p}$ and same modulus q of the relative momentum is given by the double-hatched region in fig. 2. We call this angle $2\bar{\Omega}$ and we note that it corresponds to $4\pi\omega_I$, according to the definition given in section 2. This solid angle is geometrically originated by the intersection of two hour glass-shaped angles each of which is single-hatched in fig. 2 and which we call $2\Omega_a$ and $2\Omega_b$. These angles are easily related to the momenta defined in eq. (A.1). This can be verified in Fig. 2 from which we infer that

$$\Omega_a = 2\pi(1 - \cos\theta_a)$$
$$\Omega_b = 2\pi(1 - \cos\theta_b) \qquad (A.2)$$

where

$$\cos\theta_a = \frac{p^2+q^2-k_{F>}^2}{2pq}$$

and (A.3)

$$\cos\theta_b = \frac{b^2+q^2-k_{F<}}{2bq}$$

We then immediately have that

$$4\pi\omega_S = 4\pi - 2(\Omega_a + \Omega_b - \bar{\Omega})$$
$$4\pi\omega_I = 2\bar{\Omega} \qquad (A.4)$$

The angle $\bar{\Omega}$ depends on θ_a, θ_b and on the angle θ between $\vec{b}$ and $\vec{p}$. This situation is shown more clearly in fig. A1 where the axes χ_a and χ_b are respectively parallel to $\vec{p}$ and $\vec{q}$. The solid angles Ω_a, Ω_b and $\bar{\Omega}$ are now given by the corresponding areas inscribed over the surface of a sphere of unit radius. It is clear from this figure that

i) $\bar{\Omega} = \Omega_b$ if $\theta \leq \theta_a - \theta_b \geq 0$ (A.5a)

ii) $\bar{\Omega} = \Omega_a$ if $\theta \leq \theta_b - \theta_a \geq 0$ (A.5b)

iii) $\bar{\Omega} = 0$ if $\theta \geq \theta_a + \theta_b$ (A.5c)

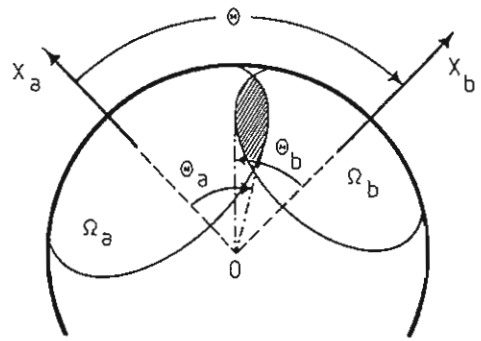

Fig.A1 - Spherical surface of unit radius over which we traced two circles originated by its intersection with the solid angles Ω_a and Ω_b. The solid angle Ω_a (Ω_b) possesses a symmetry angle θ_a (θ_b) with respect to the axis χ_a (χ_b). These axes have an angle θ between them. The shaded area is simultaneously inside Ω_a and Ω_b.

The case $|\theta_a - \theta_b| \leq \theta \leq \theta_a + \theta_b$, as it appears in fig. A2, needs a more detailed study. In Fig. A2, R and T are the centers of these circular areas, S and P are the intersection-points of the circular contours of these areas and Q is the point where the geodesic line[20] joining R and T crosses the geodesic line joining S and P. The points R, P and S define a spherical triangle of area $2A_1$. The points S, P and T define a spherical triangle of area $2A_2$. These triangles have internal angles α and β around R and T, respectively.

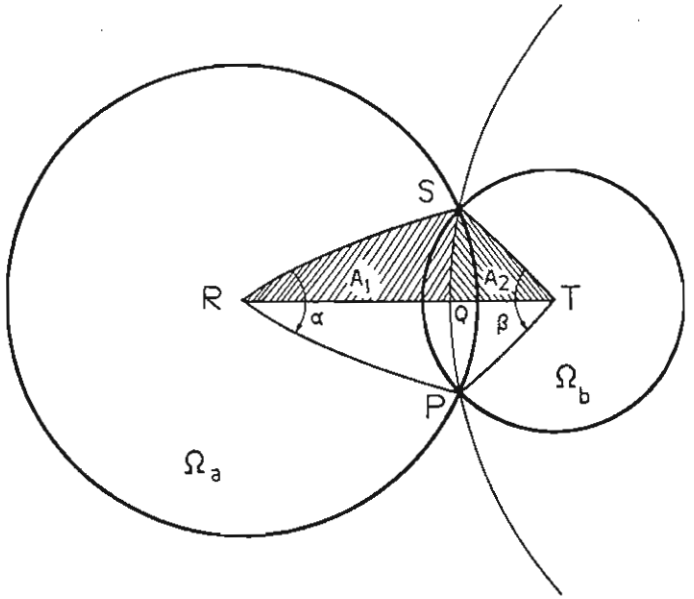

Fig. A2 - The projection into a plane of the areas Ω_a and Ω_b. R and T are their geometrical centers. S and P are the intersection points of their contours. All lines joining these points are segments of great circles over the spherical surface. A_1 and A_2 are the areas of two spherical triangles limited by some of these lines.

The part of the circular area Ω_a which is inside the lines RS and RP is equal to $\frac{\alpha}{2\pi}\ \Omega_a$. The part of the circular area Ω_b, which is inside the lines TS and TP is equal to $\frac{\beta}{2\pi}\ \Omega_b$. We then easily deduce

from fig. A2 that the intersection area between Ω_a and Ω_b is

$$\bar{\Omega} = \frac{\alpha}{2\pi}\Omega_a + \frac{\beta}{2\pi}\Omega_b - 2A_1 - 2A_2 \qquad (A.6)$$

To obtain the angle α we use two new auxiliary axes χ_p and χ_S passing by the center of the spherical surface and by the points P and S, respectively. Adopting a polar coordinate system in which χ_a is the z-axis, the angle α will be the difference between the azimuthal angles between χ_p and χ_S. In this coordinate system (θ_a,ϕ_p) and (θ,ϕ_b) are the polar and azimuthal angles corresponding to the axes χ_p and χ_b, respectively. Since the angle between χ_b and χ_p is θ_b, then

$$\cos\theta_b = \cos\theta_a \cos\theta + \sin\theta_a \sin\theta \cos(\phi_b - \phi_p)$$

from which we infer that

$$\frac{\alpha}{2} = \phi_b - \phi_p = \arccos\left[\frac{\cos\theta_b - \cos\theta\cos\theta_a}{\sin\theta\sin\theta_a}\right] \qquad (A.7)$$

Following the same lines one can find that $\beta/2$ is given by a similar equation: we must only exchange θ_a with θ_b in the above result.

The areas A_1 and A_2 can be obtained by means of a known theorem for spherical triangles, which states that

$$(\text{sum of internal angles}) - \pi = \frac{\text{area}}{R^2} \qquad (A.8)$$

where R is the radius of the spherical surface over which the triangle lays and in our case is equal to unity. For the area A_1 we deduce

$$\frac{\alpha}{2} + \xi - \frac{\pi}{2} = A_1 \qquad (A.9)$$

where ξ is the angle between the lines QS and RS. In fig. A3 we show how this area arises from the intersection of the great circles inscribed over the spherical surface. Now the z-axis is chosen so that the line QS lies on a great circle in the XY-plane and the line RQ lies

on a great circle in the plane XZ. The angle ξ will be given by the scalar product between a unitary vector perpendicular to the great circle which contains the line RS and a unitary vector in the Z-direction. In terms of the auxiliary angles θ_0 and ϕ_0, we obtain

$$\xi = \arccos\left[\frac{\sin\theta_0\sin\phi_0}{\sqrt{\cos^2\theta_0 + \sin^2\theta_0\sin^2\phi_0}}\right] \qquad (A.10)$$

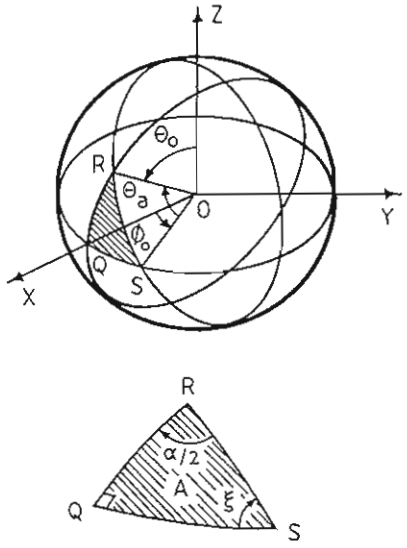

Fig. A3 - Three great circles over the spherical surface and a spherical triangle of area A limited by the segments of their intersections. With respect to a conveniently chosen coordinate-axis system, R lies on the XZ-plane and has polar coordinate θ_0, S lies on the XY-plane and has azimuthal coordinate ϕ_0. The angle between the lines joining R and S to the origin is θ_a. From this picture one deduces the internal angles $\frac{\alpha}{2}$ and ξ of the spherical triangle as functions of θ_0, ϕ_0 and θ_a.

Taking the scalar product of the same unit vector with a unit vector in the Y-direction, we find

$$\frac{\alpha}{2} = \arccos\left[\frac{\cos\theta_0\cos\phi_0}{\sqrt{\cos^2\theta_0 + \sin^2\theta_0\sin^2\phi_0}}\right] \qquad (A.11)$$

The angle θ_a is also related with θ_0 and ϕ_0 by

$$\cos\theta_a = \sin\theta_0\cos\phi_0 \qquad (A.12)$$

Eliminating θ_0 and ϕ_0 from these relations and using the equation (A.7) we obtain that

$$\frac{\pi}{2} - \xi = \arccos\left[\frac{\cos\theta_b - \cos\theta\cos\theta_a}{\sin\theta_a \sqrt{\cos^2\theta_a + \cos^2\theta_b - 2\cos\theta\cos\theta_a\cos\theta_b}}\right] \tag{A.13}$$

Substituting eqs. (A.7) and (A.13) in eq. (A.9) we reach

$$A_1 = \arccos\left[\frac{\cos\theta_b - \cos\theta\cos\theta_a}{\sin\theta\sin\theta_a}\right] - \arccos\left[\frac{\cos\theta_b - \cos\theta\cos\theta_a}{\sin\theta_a \sqrt{\cos^2\theta_a + \cos^2\theta_b - 2\cos\theta\cos\theta_a\cos\theta_b}}\right] \tag{A.14}$$

Following the same procedure one finds a similar equation for A_2: we must only exchange θ_a with θ_b in the above expression.

Gathering these results in eq. (A.6) we find finally that

$$\bar{\Omega}(\theta,\theta_a,\theta_b) = 2\arccos\left\{\cos\left[\frac{\cos\theta_b - \cos\theta\cos\theta_a}{\sin\theta \sqrt{\cos^2\theta_a + \cos^2\theta_b - 2\cos\theta\cos\theta_a\cos\theta_b}}\right] + \arccos\left[\frac{\cos\theta_a - \cos\theta\cos\theta_b}{\sin\theta_b \sqrt{\cos^2\theta_a + \cos^2\theta_b - 2\cos\theta\cos\theta_a\cos\theta_b}}\right] - \cos\theta_a \arccos\left[\frac{\cos\theta_b - \cos\theta\cos\theta_a}{\sin\theta\sin\theta_a}\right] - \cos\theta_b \arccos\left[\frac{\cos\theta_a - \cos\theta\cos\theta_b}{\sin\theta\sin\theta_b}\right]\right\} \tag{A.15}$$

for

$$|\theta_a - \theta_b| \leq \theta \leq \theta_a + \theta_b$$

To complete the calculation we note that, if $\theta_s = \theta + \theta_a + \theta_b > \pi$,

there will exist an extra intersection between the hour glass-shaped solid angles of fig. 2 and in this case the total intersection angle will be

$$\bar{\Omega}(\theta,\theta_a,\theta_b) + \bar{\Omega}(\pi-\theta,\theta_a,\theta_b) \tag{A.16}$$

with the function $\bar{\Omega}(\theta,\theta_a,\theta_b)$ given by eq. (A.15).

REFERENCES

1. For a review see: S. Nagamiya, J. Randrup and T.J.M. Symons, Ann. Rev. Nucl. Part. Sci. 155 (1984).
2. D.E. Greiner, H. Crawford, P.J. Lindstrom, J.M. Kidd, D.L. Olson, W. Schimmerling and T.J.M. Symons, Phys. Rev. C*31*, 416 (1985).
3. R.M. DeVries and J.C. Peng, Phys. Rev. C*22*, 1055 (1980).
4. D.L. Olson, B.L. Berman, D.E. Greiner, H.H. Heckman, P.J. Lindstrom, G.D. Westfall and H.J. Crawford, Phys. Rev. C*24*, 1529 (1981).
5. C.A. Bertulani and G. Baur, Nucl. Phys. A*442*, 739 (1985).
6. A. Winther and K. Alder, Nucl. Phys. A*319*, 518 (1979).
7. M.L. Goldberger, Phys. Rev. *74*, 1269 (1948).
8. E. Clementel and C. Villi, Nuovo Cimento *2*, 176 (1955).
9. N.J. DiGiacomo, R.M. DeVries and J.C. Peng, Phys. Rev. Lett. *45*, 527 (1980).
10. W.N. Hess, Rev. Mod. Phys. *30*, 368 (1958).
11. D.V. Bugg, D.C. Salter, G.H. Stafford, R.F. George, K.F. Riley and R.J. Tapper, Phys. Rev. *146*, 980 (1966).
12. E. Uehling and G. Uhlenbeck, Phys. Rev. *43*, 552 (1933).
13. J. Randrup, Nucl. Phys. A*314*, 429 (1979).
14. H.L. Bradt and B. Peters, Phys. Rev. *77*, 54 (1950).
15. Landolt-Börnstein, Vol. *I-2* (Springer, Heildelberg, 1980).
16. S.E. Koonin, Phys. Rev. Lett. *39*, 680 (1977).
17. C.F. Weizsäcker, Z. Phys. *88*, 612 (1934).
    E.J. Williams, Phys. Rev. *45*, 729 (1934).
18. A. Bohr and B. Mottelson, Nuclear Structure, Vol. *II* (Benjamin, Reading, MA, 1975).

19. J.O.T. Arruda-Neto, S.B. Herdade, I.C. Nascimento and B.L. Berman Nucl. Phys. A*389*, 378 (1982).

20. A geodesic is a line over the spherical surface that, if continued, will construct a circle whose center coincides with the center of the spherical surface. We call such circles great circles.

Resumo

Calcula-se as seções de choque em reações com íons pesados a energias de laboratório acima de 30 MeV por nucleon. Considera-se especialmente os efeitos do princípio de Pauli e das excitações eletromagnéticas. Ambos efeitos são de grande importância e foram tratados por meio de simples cálculos semiclássicos e geométricos.

Pulsar Precession: A Nod is not as Good as a Wink!

H. HEINTZMANN

Institut für Theoretische Physik der Universität Köln, Köln 51, Federal Republic of Germany

and

M. NOVELLO

Centro Brasileiro de Pesquisas Físicas, Rua Dr. Xavier Sigaud 150, Rio de Janeiro, 22290, RJ, Brasil

Recebido em 04 de fevereiro de 1986

Abstract The question of the reality of pulsar precession is reassessed and the relevant precession periods and amplitudes are reestimated. It is argued that the pulsar timing data provide evidence for the viewpoint that pulsars do indeed precess and that they turn off after some 10^4 precessional turns because they align their magnetic fields with their rotation axis due to viscous damping. Chances for an actual detection in the long known pulsars are small but PSR 1510-59 and some more recently discovered young pulsars are promising candidates.

1. INTRODUCTION

It is sometimes said that pulsars could have been predicted before their actual discovery (in 1967), but this is certainly not the case, as evidenced by the fact that even 15 years later the emission mechanism, i.e. the very basis for their detection, is still unknown and is likely to remain so for quite some time. As a matter of fact, the now generally accepted pulsar model (a rotating, magnetized neutron star) was developed in an astonishingly short time and has remained essentially unchanged since. To the very few predictions which can be made on general grounds, belong the observed slowing down of a pulsar's rotation, the unobserved internal excitations of a neutron star, such as pulsation or torsional oscillation and, last but not least, precession. All these effects have by now been observed in the case of the Earth.

As all these effects are important indicators of the global structure of a rigid body, they have received considerable attention in